

Erik Jonsson School of Engineering and Computer Science

*Energy Transfer from Colloidal Nanocrystals
to Strongly Absorbing Perovskites*

UT Dallas Author(s):

Yasiel Cabrera
Sara M. Rupich
Ryan Shaw
Benoy Anand
Manuel de Anda Villa
Rezwanur Rahman
Aaron Dangerfield
Yuri N. Gartstein
Anton V. Malko
Yves J. Chabal

Rights:

©2017 The Royal Society of Chemistry. This article may not be further made available or distributed.

Citation:

Cabrera, Yasiel, Sara M. Rupich, Ryan Shaw, Benoy Anand, et al. 2017. "Energy transfer from colloidal nanocrystals to strongly absorbing perovskites." *Nanoscale* 9(25), doi:10.1039/C7NR02234D

This document is being made freely available by the Eugene McDermott Library of the University of Texas at Dallas with permission of the copyright owner. All rights are reserved under United States copyright law unless specified otherwise.



Cite this: *Nanoscale*, 2017, 9, 8695

Energy transfer from colloidal nanocrystals to strongly absorbing perovskites†

Yasiel Cabrera,^{‡a} Sara M. Rupich,^{‡a} Ryan Shaw,^b Benoy Anand,^b Manuel de Anda Villa,^b Rezwanaur Rahman,^a Aaron Dangerfield,^a Yuri N. Gartstein,^b Anton V. Malko^b and Yves J. Chabal^{†*}

Integration of colloidal nanocrystal quantum dots (NQDs) with strongly absorbing semiconductors offers the possibility of developing optoelectronic and photonic devices with new functionalities. We examine the process of energy transfer (ET) from photoactive CdSe/ZnS core/shell NQDs into lead-halide perovskite polycrystalline films as a function of distance from the perovskite surface using time-resolved photoluminescence (TRPL) spectroscopy. We demonstrate near-field electromagnetic coupling between vastly dissimilar excitation in two materials that can reach an efficiency of 99% at room temperature. Our experimental results, combined with electrodynamics modeling, reveal the leading role of non-radiative ET at close distances, augmented by the waveguide emission coupling and light reabsorption at separations >10 nm. These results open the way to combining materials with different dimensionalities to achieve novel nanoscale architectures with improved photovoltaic and light emitting functionalities.

Received 29th March 2017,

Accepted 17th May 2017

DOI: 10.1039/c7nr02234d

rsc.li/nanoscale

Introduction

Combining organic and inorganic semiconductors at the nanoscale offers attractive opportunities to develop novel optoelectronics and photonic architectures that may be used to judiciously explore the advantages of both classes of materials. Among various schemes to manipulate excitation in such hybrid structures, the concept of the excitonic energy transfer (ET) has been gaining research attention. First proposed by Agranovich and co-workers¹ for semiconductor quantum well/organic overlayer hybrids, this concept has been demonstrated in a variety of geometries, including between nanocrystal quantum dots (NQDs) and semiconductor, organic, or two-dimensional (2D) materials.^{2–11} Several recent reviews have described the applications of energy transfer schemes for various optoelectronics applications including photovoltaics (PVs), light-emitting diodes (LEDs) and sensors.^{12–16}

At the same time, the emergence of strongly absorbing organometallic halide perovskite materials has occurred. These materials are characterized by strong broadband absorption, long charge carrier diffusion lengths, and low processing

costs. They are therefore widely used for PV applications,^{17–19} but are also relevant for LEDs, tunable nanolasers, photo-detectors and thin film transistors.^{5,20–24} The strong light-matter interactions found in perovskites make them attractive for energy coupling with other optically active subsystems, including the coherent interaction between tightly confined (Frenkel) excitons found in quantum-confined NQDs and weakly confined (Wannier-Mott) excitons characteristic of bulk semiconductors.¹⁶ Surprisingly, there has not been any attempt to detect exciton flow *via* near-field electromagnetic interactions in NQD/perovskite hybrids to date, despite the importance of this process.

In this paper, we investigate (incoherent) near-field electromagnetic energy transfer between core-shell CdSe/ZnS NQDs and strongly absorbing polycrystalline methylammonium lead halide (CH₃NH₃PbI₃) perovskites. We employ atomic layer deposition (ALD) to deposit thin Al₂O₃ layers on top of perovskite thin films as inert spacers of controllable thickness. We bring to bear extensive characterization of the perovskite films to monitor their integrity and measure ET rates in NQD/perovskite hybrids as a function of the NQD's distance from the perovskite layer. We show, *via* time-resolved (TR) photoluminescence (PL) spectroscopy, a greater than 20-fold acceleration of the NQD donor's PL decay in hybrid samples compared to the reference NQD/glass sample. Combined with detailed electromagnetic modeling, our results show that the efficiency of non-radiative energy transfer (NRET) can approach >99% for a hybrid system where the NQDs are located directly on the perovskite layer. This is the highest

^aDepartment of Material Science & Engineering, The University of Texas at Dallas, Richardson, TX 75080, USA. E-mail: chabal@utdallas.edu

^bDepartment of Physics, The University of Texas at Dallas, Richardson, TX 75080, USA

† Electronic supplementary information (ESI) available. See DOI: 10.1039/c7nr02234d

‡ These authors contributed equally to the work.

NRET efficiency reported in the literature for any type of semiconductor acceptor material. When the total separation between NQD and perovskite is ~ 15 nm (measured from the center of the NQD to the perovskite surface), an ET efficiency of $\sim 65\%$ is observed due to the combined effects of non-radiative ET and radiative waveguide coupling. Such high ET efficiencies and large effective interaction distances establish perovskites as exceptional energy accepting materials, suitable for the implementation of exciton and multiexciton²⁵ harvesting from optically thick NQD solids into technologically relevant PV materials.

Experimental

Materials

Cadmium oxide (99.99%), 1-octadecene (90%), octadecylamine (97%), oleic acid (90%), selenium (99.999%), sulfur (99.998%), trioctylphosphine oxide (99%), zinc oxide (99.99%), hydroiodic acid (HI, 57 wt% in H₂O), methylamine (33% in ethanol), diethyl ether (anhydrous, 99.0%), ethanol (200 proof), lead iodide (PbI₂, 99.999%), *N,N*-dimethylformamide (DMF), trimethylaluminum (TMA), and sulfuric acid (95%) were purchased from Sigma-Aldrich. Poly(methyl) methacrylate (PMMA, MW = 950 000 g mol⁻¹, 2% in aniline) was purchased from Microchem. Hydrogen peroxide (30%) was purchased from JT Baker. Octadecylphosphonic acid (99%) was from PCI Synthesis and trioctylphosphine (TOP, 97%) from Strem. Solvents were purchased from Fisher. Nanopure deionized water (dH₂O, $\rho = 18$ M Ω cm) was obtained *via* a Millipore system.

Methylammonium lead iodide (CH₃NH₃PbI₃) perovskite thin films

Methylammonium iodide (CH₃NH₃I) was synthesized according to literature procedures.^{26,27} In brief, HI (10 mL) was added to a solution of methylamine (24 mL) at 0 °C and stirred for 2 h. The white precipitate was isolated by vacuum filtration, washed with diethyl ether and purified (2 \times) by recrystallization in ethanol. CH₃NH₃PbI₃ films were prepared using a vapor-assisted solution process (VASP) in a N₂-purged glovebox. First, PbI₂ (200 mg mL⁻¹ in DMF) was spun-cast (60 s at 1.5 krpm) onto piranha cleaned glass coverslips (18 \times 18 mm). The films were dried on a hot plate at 150 °C for 15 min and then treated with CH₃NH₃I vapor based on a modified VASP.²⁸ In brief, the sample was suspended 2 cm above the CH₃NH₃I powder as shown schematically in Fig. S1.† Both the powder and the sample were heated to 160 °C for 90 min. Upon completion, the samples were cut in half for further passivation and characterization. Samples were either used as is or coated with PMMA or Al₂O₃ to enhance air stability. PMMA was spun-cast (60 s at 2 krpm) on the perovskites and the samples were dried on a hot plate at 80 °C for 2 min.

Atomic layer deposition of Al₂O₃

Al₂O₃ layers were deposited at 80 °C using TMA and DI-H₂O on a Cambridge Nanotech Savannah 100 system. The films were

first dosed with 10 pulses of TMA followed by full cycles of TMA and H₂O pulses until the desired thickness was achieved (70 cycles for 5–6 nm films, and 160 cycles for 11.5 nm films). For longer depositions, the precursors had a pulse time of 0.015 s and a purge time of 40 s, while for the shorter processes a 30 s purge time was used. The chamber pressure was kept at ~ 0.5 Torr with a constant N₂ flow of 20 sccm. All depositions occurred on perovskite films as well as on a reference silicon substrate for thickness calibration. Additionally, ALD was carried out in a home-built reactor for *in situ* analysis as described in the ESI.†

NQD synthesis and deposition

CdSe NQDs were prepared based on literature methods with a minor modification: the injected volume of TOP was doubled.²⁹ Core-shell NQDs, 2 CdS and 4 ZnS shells were prepared according to the SILAR technique.^{30,31} NQD layers were deposited by spin-casting (2.5 mg mL⁻¹ in toluene, 60 s at 2 krpm) in a N₂-purged glovebox on various substrates including glass slides, Al₂O₃ passivated perovskites and bare perovskites.

Characterization techniques

X-ray diffraction (XRD) spectra were recorded using $2\theta/\omega$ scans on a Rigaku Ultima III X-ray diffractometer system with a Cu-K α source ($\lambda = 0.154$ nm) at 44 kV and 40 mA. AFM images were collected on a Veeco Digital Instrument Nanoscope Dimension 3100 in tapping mode. Root-mean-square roughness and film thickness were determined using Gwyddion software. UV-Vis absorbance measurements were collected in transmission mode using an Agilent Cary 5000 UV-Vis-NIR spectrometer. Ellipsometry measurements were taken with a Horiba Jobin UVISSEL ellipsometer and the data were fit in DeltaPsi2 software. Fourier Transform Infrared (FTIR) measurements were performed in transmission at Brewster's angle ($\sim 70^\circ$) in a Thermo Nicolet 6700 spectrometer equipped with a MCT-B detector. X-ray photoemission spectroscopy (XPS) was performed on a Quantum 2000 Scanning ESCA microprobe spectrometer (Physical Electronics) equipped with a monochromatic Al K $\alpha_{1,2}$ -radiation source and a concentric hemispherical analyzer under ultrahigh vacuum conditions (10⁻⁹ mbar). PL measurements were carried out using a microscope-based time-resolved PL system based on an Olympus IX71 inverted microscope. Samples were excited at 405 nm (300 fs) generated by frequency-doubling the output of a Ti:Sapphire pulsed laser (MIRA 900F) focused on the sample surface using a NA = 0.9 objective. The emission, collected using the same objective, was passed through a spectrometer to a silicon avalanche photodiode (MicroPhotonDevices). TRPL was measured using time-correlated single photon counting (PicoQuant 300 GmbH).

Results and discussion

A schematic of the physical system (NQDs, perovskite film and glass substrate) is shown in Fig. 1(a). To study ET from NQDs

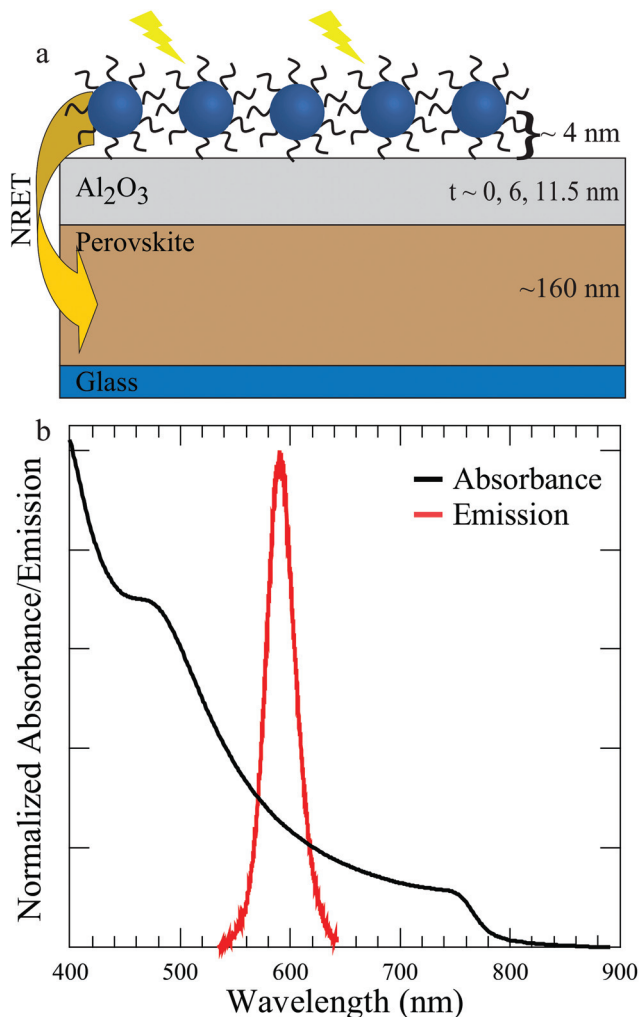


Fig. 1 (a) Schematic of the hybrid structure showing the energy transfer from the NQDs to the perovskite layer. Thickness (t) of the Al_2O_3 spacer layer is varied from 0 nm, no oxide, to ~ 11.5 nm. A single layer of NQDs was spun-cast on the ~ 160 nm thick perovskite film supported on a glass coverslip. ET into the perovskite was measured by TRPL spectroscopy. ET occurs through both NRET and RET. (b) UV-visible absorbance of the $\text{CH}_3\text{NH}_3\text{PbI}_3$ perovskite film on glass as well as the PL emission of a monolayer of close-packed CdSe/ZnS NQDs spun-cast on glass.

to the perovskite film, sufficient spectral overlap between the NQD emission and perovskite absorption is needed. Fig. 1(b) shows the PL emission spectrum of the NQD films on glass and the UV-vis absorbance spectra of the lead halide perovskite. The NQDs have a sharp and fairly narrow emission, peaking at ~ 590 nm, which overlaps with the strong, broad band absorption of the $\text{CH}_3\text{NH}_3\text{PbI}_3$ perovskite film. Therefore energy transfer is possible.

To prepare the hybrid samples, the perovskite was synthesized using a modified VASP method at 160°C for 90 min, which resulted in the formation of an orthorhombic crystal structure as seen in Fig. 2(a). Then, a solution of oleic acid capped CdSe/ZnS NQDs was spun-cast onto either a bare perovskite film or an Al_2O_3 encapsulated perovskite film.

Additionally, NQDs deposited on a glass coverslip were used as a reference sample. The total distance between the center of the NQDs and perovskite is controlled by the thickness (t) of the Al_2O_3 spacer layer (0 nm, no Al_2O_3 , to ~ 5 – 6 and 11.5 nm with Al_2O_3). The diameter of the NQDs (total diameter of ~ 7 – 8 nm including the ligand shell) is determined from TEM (Fig. S2†) while the thickness of the Al_2O_3 layer is calculated from IR absorption measurements of the TO and LO phonons of Al_2O_3 , calibrated by ellipsometry on reference silicon substrates.

As perovskites are highly sensitive to the environment, in particular to water, their synthesis and subsequent processing is delicate, requiring thorough characterization to ensure that their integrity is not degraded. These issues become important when the methods used to deposit NQDs at specific distances from the substrate involve processes that could alter the perovskite film. Ideally, we would like to control the distance between the perovskite and the NQDs by using a spacer layer that does not damage the perovskite's integrity, is not miscible with the NQD solution (*i.e.*, must be deposited from orthogonal solvents), protects the perovskite during subsequent wet-chemical treatments, and is optically transparent over the region of interest. In this respect, PMMA is not appropriate as it is miscible with the NQDs and thus the thickness cannot be controlled. Instead, deposition of a metal oxide (Al_2O_3) spacer layer *via* ALD appears best for these requirements because ALD is a low temperature process that is usually gentle with the substrate. In fact, Al_2O_3 encapsulation of perovskite films by ALD has been shown to increase air stability as well as photovoltaic performance.^{32–36} However, depositions must be done with care to prevent back-conversion of the perovskite to PbI_2 . While some groups found that standard deposition procedures with TMA and O_3 or H_2O work at low temperatures,^{33,36} others found that non-hydrolytic processes are needed to maintain the integrity of the perovskite.³²

We have therefore explored ALD of Al_2O_3 on perovskite films in detail. We find that using standard TMA/ H_2O cycles at 80°C results in complete back-conversion to PbI_2 (Fig. S3(a)†). However, if the surface was first dosed with 10 pulses of TMA before full TMA/ H_2O cycles were performed, the integrity of the sample is preserved. In the later case, only minor PbI_2 formation is observed as shown in Fig. S3(b),† which is tentatively attributed to a temperature effect (*i.e.* time spent at elevated temperature) during the Al_2O_3 growth.^{37,38} This hypothesis was checked experimentally using *in situ* FTIR spectroscopy. Fig. S4† clearly shows changes in the perovskite absorption as a function of time spent at 80°C ; however, the changes are relatively small on the time scales (<2 h) needed for the commercial ALD reactor used to deposit the spacer layer. Importantly, UV-visible absorption of the perovskite film remains essentially unchanged (Fig. 2(b)). Since the absorption of the acceptor is the critical factor for energy transfer, not the PL, the small decrease of PL lifetime upon Al_2O_3 growth (Fig. S5†) will not affect the analysis of the data or the validity of the study. For example, Si has a poor PL QY; however it is an efficient energy acceptor.^{6–8}

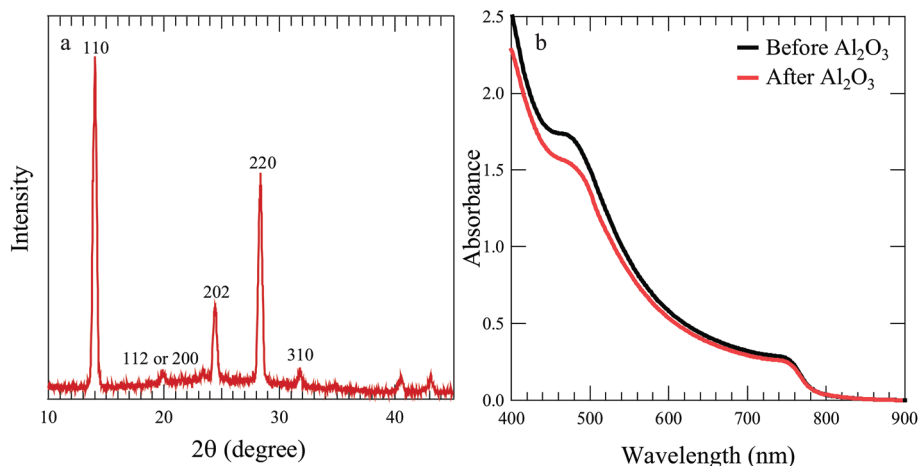


Fig. 2 (a) X-ray diffraction pattern of a $\text{CH}_3\text{NH}_3\text{PbI}_3$ perovskite prepared at 160 °C for 90 min. The main phases are labeled. (b) UV-visible absorbance of the lead halide perovskite before and after Al_2O_3 growth.

The growth of Al_2O_3 on the perovskite is verified by the appearance of the Al_2O_3 TO/LO phonon modes *via in situ* FTIR spectroscopy (Fig. S6†) and the Al peak *via ex situ* XPS (Fig. S7†). The analysis of the Al_2O_3 TO/LO modes on both perovskite and silicon with native oxide reveals that the Al_2O_3 film grows at the same rate on both surfaces. The average thickness can therefore be determined from ellipsometry measurements on reference silicon samples, and carried over for films grown on perovskite samples where ALD was done in the same chamber and at the same time as on reference Si samples (Fig. S6†). We find that Al_2O_3 spacer layers of 5.1 ± 0.2 nm and 11.5 ± 0.4 nm are obtained for films grown from 70 and 160 cycles, respectively. Due to the textured surface of the perovskite (Fig. S7(b)†), this is an estimate of the average thickness over the sample.

Hybrid NQD/perovskite samples were prepared by depositing NQDs on the surface of the perovskite, either bare or Al_2O_3 passivated. Among the many possible methods for depositing NQDs on substrates,^{6,12,39–42} we select spin-casting of colloidal NQDs in toluene in this case in order to obtain uniform and controllable coverage without damaging the perovskite. By controlling the concentration, close to a monolayer of close-packed NQDs was deposited as determined from AFM of NQDs spun-cast on a reference flat substrate (Fig. S8(a)†).

To assess the energy transfer from the NQDs into the perovskite films, the hybrid samples were characterized *via* TRPL decay measurements as a function of Al_2O_3 spacer thicknesses. While PL monitoring is commonly used in studies of Förster-type ET involving point-to-point interaction of molecular entities, its application in layered systems is subject to many constraints. The absolute value of the PL intensity in a μPL system is affected by the specifics of excitation and collection geometries due to non-uniform sample coverage, interference in multilayered structures and directionality of the radiative emission patterns. PL dynamics, on the other hand, provide direct insight into the relaxation pathways present in the hybrid

samples, irrespective of the above influences.^{6,12,43} In our case, the detected PL intensity is low due to both substantial ET in the NQD/perovskite hybrids and the relatively low number of NQD donors. To overcome this difficulty, a microscope based TRPL system (μPL) was employed, which allows for tight light focusing and collection.

Due to the close-packed nature of the NQD monolayers, spectral diffusion between neighboring NQDs is present; therefore, the lifetime of the NQDs is measured on the red side of the emission spectrum which is not affected (Fig. S9†).¹² To assess the contribution of radiative and non-radiative ET, the PL lifetime of the donor NQDs (measured at ~ 605 nm) in hybrid samples with different Al_2O_3 spacer thicknesses (0 nm, 5–6 nm and 11.5 nm) is compared to that of NQD monolayers on glass as shown in Fig. 3(a). The NQD PL dynamics in the hybrids differ, with the fastest lifetimes on bare perovskites. To improve accuracy, several samples of each kind were prepared, resulting in 5–30 PL lifetime measurements for each spatial separation. The representative traces in Fig. 3(a) are all fit to monoexponential decays, with the statistical average of NQD PL lifetimes on bare perovskite yielding $\tau_{\text{bare}} \sim 1$ ns; on 5–6 nm Al_2O_3 spacer, $\tau_{5\text{ nm}} \sim 4$ ns; on 11.5 nm Al_2O_3 spacer, $\tau_{11\text{ nm}} \sim 9$ ns, and for reference NQDs on glass, $\tau_{\text{NQD}} \sim 21$ ns. The statistical distribution of the experimentally measured PL decay rates is reflected in the error bars as shown in Fig. 3(b). From the measured PL lifetimes, the calculated acceleration of the NQD decay rates in the hybrids, $\Gamma/\Gamma_{\text{glass}}$ (where $\Gamma = 1/\tau$), as compared to decays on glass is computed for the three spacer thicknesses and are shown as black dots in Fig. 3(b).

The experimental data can be rationalized with the help of the well-known macroscopic electrodynamics framework^{44,45} developed to describe the effect of stratified substrates on the electromagnetic decay of electric-dipole emitters. This framework was successfully applied to a variety of systems, including in our earlier studies of ET from NQDs to silicon and 2D semiconductors.^{6,11,46,47} As a result of the electromagnetic

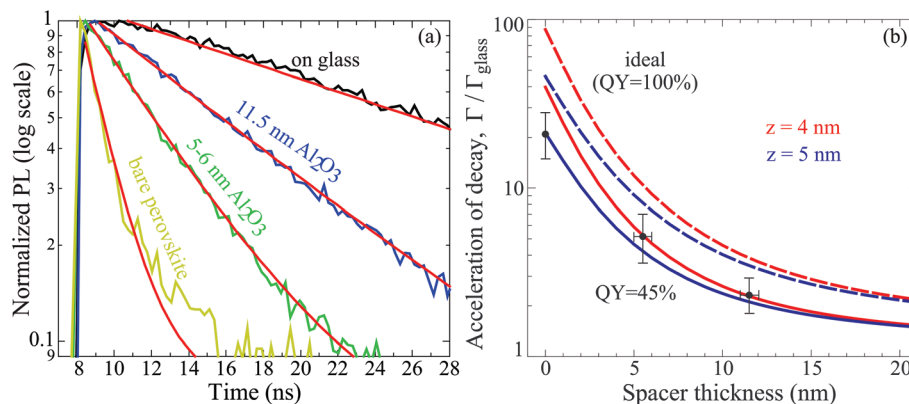


Fig. 3 (a) NQD PL decay times for hybrids with different Al_2O_3 spacer thicknesses ($t = 0, 5\text{--}6, 11.5$ nm) on the perovskite as well as on a glass slide as a reference. All lifetimes were measured on the red side of the NQD emission spectrum (~ 605 nm). PL lifetimes (τ) were determined from mono-exponential fits to the data, shown as red lines. (b) Calculated sets of enhancement ratios as a function of the Al_2O_3 spacer thickness for two different representative NQD-to-surface distances, $z = 4$ nm (red) and $z = 5$ nm (blue) and for two values of the NQD QY, idealistic 100% (dashed lines) and more realistic, QY = 45% (solid lines). Black dots – experimental values extracted from the PL lifetime measurements, error bars – statistical standard deviation. The perovskite slab thickness used in the computations is 160 nm.

interaction with the substrate, the spontaneous vacuum (air) decay rate Γ_0 of the randomly oriented emitter is modified to Γ^{id} as follows:

$$\Gamma^{\text{id}}/\Gamma_0 = 1 + F(0, \infty), \quad (1)$$

$$F(a, b) = \text{Re} \int_a^b \frac{s ds}{2\sqrt{1-s^2}} \left[(2s^2 - 1)r^{(\text{p})}(s) + r^{(\text{s})}(s) \right] \times \exp(2ik_0z\sqrt{1-s^2}). \quad (2)$$

In eqn (2), the parameters are the vacuum wavenumber k_0 , the electric-dipole (center of NQD) distance, z , to the substrate and variable $s = k_{\parallel}/k_0$, the ratio of the conserved in-plane wave-vector component, k_{\parallel} , and k_0 . Eqn (1) describes all radiative and non-radiative processes that are due to the substrate properties encompassed in the reflection amplitudes, $r^{(\text{p})}$ and $r^{(\text{s})}$, for p- and s-polarized waves.⁴⁵ With these equations, one can compute the decay rate of the NQD emitter on the pure glass substrate, $\Gamma_{\text{glass}}^{\text{id}}$, as well as the decay rate, Γ^{id} , on our layered structure: Al_2O_3 spacer/perovskite slab/glass. The resulting decay acceleration ratio, $\Gamma^{\text{id}}/\Gamma_{\text{glass}}^{\text{id}}$, is shown in Fig. 3(b) by dashed lines as a function of the spacer thickness for two values of the NQD distance, z , to the top surface of the structure. The optical properties (at 606 nm) of the structure materials employed in the computation are as follows: glass refraction index, $n_{\text{glass}} = 1.5$, spacer refraction index, $n_{\text{spacer}} = 1.77$, and complex-valued dielectric function of the perovskite⁴⁸ slab $\epsilon_s = 7.02 + i1.31$. For proper comparison with experiments, one also needs to take into account “local” non-radiative decay⁴⁶ processes (rate Γ_{nr}), such as those leading to the less than perfect emission quantum yield (QY) or caused by spectral diffusion: these processes add to the “ideal” decay rates in eqn (1). The observed decay rate on glass becomes $\Gamma_{\text{glass}} = \Gamma_{\text{glass}}^{\text{id}} + \Gamma_{\text{nr}}$, and we quantify additional non-radiative processes using the generalized QY for the decay on the

glass substrate *via* $\Gamma_{\text{nr}} = \Gamma_{\text{glass}}^{\text{id}}(1 - \text{QY})/\text{QY}$. In our earlier experiments⁴⁶ with similar NQDs, we established a NQD QY in solution of $\sim 55\%$, which reduces slightly to QY $\sim 45\text{--}50\%$ upon deposition on glass. The solid lines in Fig. 3(b) show the expected acceleration ratio, $\Gamma/\Gamma_{\text{glass}}$, if QY = 45% is used in the computations. The resulting modelling curves are in good agreement with the experimentally observed trend. The computational results are very sensitive to the separation distance at small spacer thicknesses, and it is understandable that the no-spacer experimental point is better represented by a somewhat larger $z = 5$ nm curve – the theoretical model assumes ideal planar material slabs while the actual perovskite surface features variations from planarity (Fig. S8(b)†).

The overall good agreement of the experimental data with the computational results provides evidence supporting ET from the NQDs into the perovskite layer as the mechanism for the observed PL lifetime quenching. By the same token, the charge transfer mechanism must then be excluded as a noticeable contributor. Charge transfer is facilitated by the overlap of the electronic wave-functions and depends exponentially on angstrom-size distances. The observed nanometer scale distance dependence on the PL lifetime clearly advocates for energy, and not charge, transfer mechanisms. Any substantial contribution from charge transfer would lead to a faster acceleration decay for NQDs placed directly on the perovskite layer than was observed.

While quantitatively explaining the experimentally measured data, the same theoretical model can provide further insight into the role of (and opportunities for) various processes that realize ET from NQDs into the underlying semiconductor layer. Fig. 4 illustrates those as affected by the dielectric function $\epsilon_s = \epsilon'_s + i\epsilon''_s$ of the energy acceptor slab and shows a comparison of the results for perovskite ($\epsilon_s = 7.02 + i1.31$)⁴⁸ and silicon ($\epsilon_s = 15.44 + i0.15$)⁴⁹ slabs in the same geometrical structure. The overall electromagnetic decay rate, given in eqn (1),

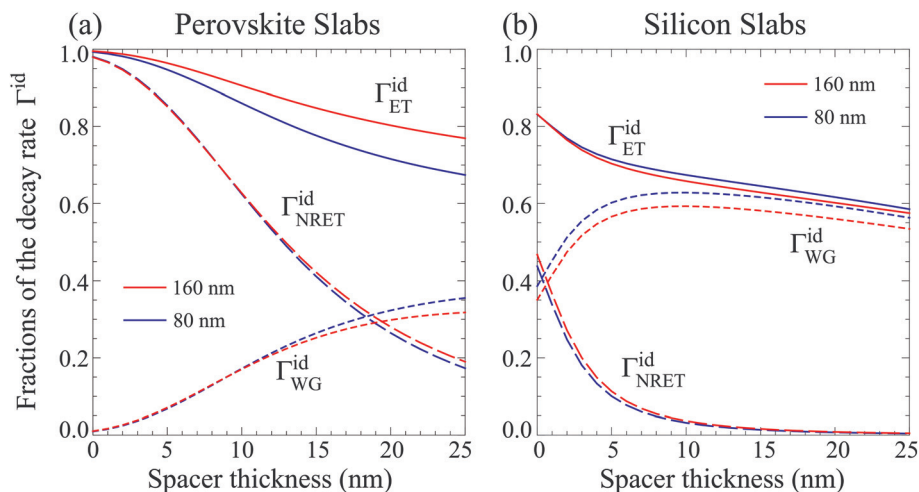


Fig. 4 Relative contributions to the electromagnetic decay rate, eqn (1), of the randomly oriented NQD emitter on the top of the spacer/energy acceptor slab/glass structures for $z = 4$ nm and wavelength of 606 nm: total ET into the absorbing slab (solid curves), non-radiative ET (NRET, dashed curves) and the emission of waveguiding photonic modes (short-dashed curves). Red curves are for the slab thickness of 160 nm and blue curves for the thickness of 80 nm. (a) Computational results for the perovskite acceptor slab with $\epsilon_s = 7.02 + i1.31$ and (b) for the silicon acceptor slab with $\epsilon_s = 15.44 + i0.15$.

includes decay into photons that are emitted into air (rate Γ_{\uparrow}) and into the bottom glass substrate (rate Γ_{\downarrow}). Those decay channels need to be deducted from the measured rate:

$$\Gamma_{\text{ET}}^{\text{id}} = \Gamma^{\text{id}} - \Gamma_{\uparrow} - \Gamma_{\downarrow}, \quad (3)$$

to obtain the total ET rate that includes all contributions to energy transfer into the semiconductor slab. The calculations of Γ_{\uparrow} and Γ_{\downarrow} are described in ref. 45 and detailed in our earlier work.¹¹ Fig. 4 shows (solid lines) the resulting fraction $\Gamma_{\text{ET}}^{\text{id}}/\Gamma^{\text{id}}$ due to ET, thereby constituting the ideal efficiency of ET for the given structure configuration. This ideal efficiency would be reduced if the QY is less than 100%. Further distinctions can be made by assessing contributions represented by eqn (2) for different ranges of the in-plane wave vectors. In particular, $F(\sqrt{\epsilon'_s}, \infty)$ corresponds to the range of wave vectors, where no propagating waves can exist, it thus describes NRET.^{6–8,12,43,46,47} On the other hand, $F(n_{\text{glass}}, \sqrt{\epsilon'_s})$ corresponds to the range of wave vectors, where wave propagation can occur only within the slab, it therefore describes ET *via* emission of wave-guiding (WG) modes. The resulting fractions: $\Gamma_{\text{NRET}}^{\text{id}}/\Gamma^{\text{id}}$ and $\Gamma_{\text{WG}}^{\text{id}}/\Gamma^{\text{id}}$ are shown in Fig. 4 by dashed and short-dashed lines, respectively. It should be noted that for strongly absorbing medium, the boundaries between the different regions are somewhat blurred but are still representative. Fig. 4(a) and (b) demonstrate the stark difference between the roles of different contributions to ET that takes place for the perovskite and silicon layers at 606 nm. While the WG channel dominates over NRET in silicon beginning at very thin spacers, the strong absorption in the perovskite retains NRET as dominant for spacers up to ~ 15 nm. For the same reason of large ϵ''_s , the overall ET into the perovskite is also effected by the absorption of “ordinary” photons emitted by NQDs that would propagate in the whole space experiencing refraction at

the interfaces of the structure under consideration. This contribution is clearly seen in Fig. 4(a) for the thickest spacers ($\Gamma_{\text{ET}}^{\text{id}} > \Gamma_{\text{NRET}}^{\text{id}} + \Gamma_{\text{WG}}^{\text{id}}$) and becomes smaller for thinner slabs (compare the results for 160 nm and 80 nm thick perovskite slabs).

Very high NRET rates lead to extremely high efficiencies of ET into the perovskite material even for appreciably thick spacers. To exemplify these rates for the three spacers used in the experimental work, the modelling results derived for $z = 4$ nm ($z = 5$ nm) separation and a wavelength of 606 nm yield ideal ET efficiencies of 99.5% (99.1%), 95.4% (94.2%) and 89.3% (88.1%) for the spacers of 0, 5–6, and 11.5 nm thicknesses, respectively. For the NQD with QY = 45% on glass, those ET efficiency values reduce to 98.1% (96.5%), 84.2% (80.1%) and 68.7% (65.9%) respectively. It should be emphasized that efficient ET greatly increases the extraction of excitons from NQDs as ET into the acceptor semiconductor occurs faster than parasitic local non-radiative processes. The extremely high ET efficiency numbers derived above, along with the strong absorption in the broad spectral region clearly qualify the perovskites as exceptional energy accepting materials.

Conclusions

We have described the chemical preparation, materials characterization and optical performance of hybrid NQD/ Al_2O_3 /perovskite layered nanoscale materials. ALD-grown Al_2O_3 spacers have been used to modulate the strength of the near-field electromagnetic interactions between the components. Using TRPL spectroscopy, we find a 20-fold acceleration of the PL lifetime for NQDs placed on perovskites, indicative of strong ET. Combined with electrodynamics modeling, the results confirm highly efficient non-radiative energy transfer,

the efficiency of which can reach 99%. For large NQD-to-perovskite separation (~ 15 nm), a combination of NRET and waveguide coupling retains the efficiency at $\sim 65\%$, underscoring a strong light-matter interaction with perovskite materials. The ability to achieve strong near-field electromagnetic interactions between dissimilar semiconductor materials presents an exciting opportunity for developing new types of functional nanomaterials for photonic applications. Such schemes are especially promising for efficient multiexciton harvesting from NQD solids,²⁵ potentially augmenting the performance of the perovskite solar cells above the Shockley-Queisser limit. It also opens the opportunity to possibly reach the strong coupling limit, for which the hybridization of Frenkel and Wannier-Mott excitons was envisioned to lead to enhanced non-linear properties.^{16,50}

Acknowledgements

We thank David Mueller for his help in carrying out the PL measurements. This work was financially supported by the National Natural Science Foundation (NSF) under the ECCS-CAREER Award # 1350800.

Notes and references

- D. Basko, G. C. La Rocca, F. Bassani and V. M. Agranovich, *Eur. Phys. J. B*, 1999, **8**, 353–362.
- M. Achermann, M. A. Petruska, S. Kos, D. L. Smith, D. D. Koleske and V. I. Klimov, *Nature*, 2004, **429**, 642–646.
- T. A. Klar, T. Franzl, A. L. Rogach and J. Feldmann, *Adv. Mater.*, 2005, **17**, 769–773.
- S. Lu and A. Madhukar, *Nano Lett.*, 2007, **7**, 3443–3451.
- Q. Zhang, T. Atay, J. R. Tischler, M. S. Bradley, V. Bulovic and A. V. Nurmikko, *Nat. Nanotechnol.*, 2007, **2**, 555–559.
- H. M. Nguyen, O. Seitz, D. Aureau, A. Sra, N. Nijem, Y. N. Gartstein, Y. J. Chabal and A. V. Malko, *Appl. Phys. Lett.*, 2011, **98**, 161904.
- H. M. Nguyen, O. Seitz, W. Peng, Y. N. Gartstein, Y. J. Chabal and A. V. Malko, *ACS Nano*, 2012, **6**, 5574–5582.
- M. T. Nimmo, L. M. Caillard, W. De Benedetti, H. M. Nguyen, O. Seitz, Y. N. Gartstein, Y. J. Chabal and A. V. Malko, *ACS Nano*, 2013, **7**, 3236–3245.
- Z. Chen, S. Berciaud, C. Nuckolls, T. F. Heinz and L. E. Brus, *ACS Nano*, 2010, **4**, 2964–2968.
- F. Prins, A. J. Goodman and W. A. Tisdale, *Nano Lett.*, 2014, **14**, 6087–6091.
- S. Sampat, T. Guo, K. Zhang, J. A. Robinson, Y. Ghosh, K. P. Acharya, H. Htoon, J. A. Hollingsworth, Y. N. Gartstein and A. V. Malko, *ACS Photonics*, 2016, **3**, 708–715.
- W. Peng, S. M. Rupich, N. Shafiq, Y. N. Gartstein, A. V. Malko and Y. J. Chabal, *Chem. Rev.*, 2015, **115**, 12764–12796.
- B. Guzelturk and H. V. Demir, *Adv. Funct. Mater.*, 2016, **26**, 8158–8177.
- S. V. Kershaw, L. Jing, X. Huang, M. Gao and A. L. Rogach, *Mater. Horiz.*, 2017, **4**, 155–205.
- N. Kholmicheva, P. Moroz, H. Eckard, G. Jensen and M. Zamkov, *ACS Energy Lett.*, 2017, **2**, 154–160.
- V. M. Agranovich, Y. N. Gartstein and M. Litinskaya, *Chem. Rev.*, 2011, **111**, 5179–5214.
- M. Gratzel, *Nat. Mater.*, 2014, **13**, 838–842.
- M. A. Green and T. Bein, *Nat. Mater.*, 2015, **14**, 559–561.
- M. A. Green, A. Ho-Baillie and H. J. Snaith, *Nat. Photonics*, 2014, **8**, 506–514.
- S. D. Stranks and H. J. Snaith, *Nat. Nanotechnol.*, 2015, **10**, 391–402.
- Z.-K. Tan, R. S. Moghaddam, M. L. Lai, P. Docampo, R. Higler, F. Deschler, M. Price, A. Sadhanala, L. M. Pazos, D. Credgington, F. Hanusch, T. Bein, H. J. Snaith and R. H. Friend, *Nat. Nanotechnol.*, 2014, **9**, 687–692.
- X. Y. Chin, D. Cortecchia, J. Yin, A. Bruno and C. Soci, *Nat. Commun.*, 2015, **6**, 7383.
- L. Dou, Y. Yang, J. You, Z. Hong, W.-H. Chang, G. Li and Y. Yang, *Nat. Commun.*, 2014, **5**, 5404.
- H. Zhu, Y. Fu, F. Meng, X. Wu, Z. Gong, Q. Ding, M. V. Gustafsson, M. T. Trinh, S. Jin and X. Y. Zhu, *Nat. Mater.*, 2015, **14**, 636–642.
- T. Guo, S. Sampat, S. M. Rupich, J. A. Hollingsworth, H. Htoon, Y. J. Chabal, Y. N. Gartstein and A. V. Malko, *ACS Nano*, (submitted).
- Q. Chen, H. Zhou, Z. Hong, S. Luo, H.-S. Duan, H.-H. Wang, Y. Liu, G. Li and Y. Yang, *J. Am. Chem. Soc.*, 2014, **136**, 622–625.
- M. Liu, M. B. Johnston and H. J. Snaith, *Nature*, 2013, **501**, 395–398.
- C. Liu, J. Fan, X. Zhang, Y. Shen, L. Yang and Y. Mai, *ACS Appl. Mater. Interfaces*, 2015, **7**, 9066–9071.
- L. Carbone, C. Nobile, M. De Giorgi, F. D. Sala, G. Morello, P. Pompa, M. Hytch, E. Snoeck, A. Fiore, I. R. Franchini, M. Nadasan, A. F. Silvestre, L. Chiodo, S. Kudera, R. Cingolani, R. Krahne and L. Manna, *Nano Lett.*, 2007, **7**, 2942–2950.
- J. J. Li, Y. A. Wang, W. Z. Guo, J. C. Keay, T. D. Mishima, M. B. Johnson and X. G. Peng, *J. Am. Chem. Soc.*, 2003, **125**, 12567–12575.
- R. G. Xie, U. Kolb, J. X. Li, T. Basche and A. Mews, *J. Am. Chem. Soc.*, 2005, **127**, 7480–7488.
- I. S. Kim and A. B. F. Martinson, *J. Mater. Chem. A*, 2015, **3**, 20092–20096.
- X. Dong, X. Fang, M. Lv, B. Lin, S. Zhang, J. Ding and N. Yuan, *J. Mater. Chem. A*, 2015, **3**, 5360–5367.
- C.-Y. Chang, K.-T. Lee, W.-K. Huang, H.-Y. Siao and Y.-C. Chang, *Chem. Mater.*, 2015, **27**, 5122–5130.
- M. Kot, C. Das, Z. Wang, K. Henkel, Z. Rouissi, K. Wojciechowski, H. J. Snaith and D. Schmeisser, *ChemSusChem*, 2016, **3**, 3401–3406, DOI: 10.1002/cssc.201601186.

- 36 D. Koushik, W. J. H. Verhees, Y. Kuang, S. Veenstra, D. Zhang, M. A. Verheijen, M. Creatore and R. E. I. Schropp, *Energy Environ. Sci.*, 2017, **10**, 91–100.
- 37 L.-C. Chen, C.-C. Chen, J.-C. Chen and C.-G. Wu, *Sol. Energy*, 2015, **122**, 1047–1051.
- 38 B. Conings, J. Drijkoningen, N. Gauquelin, A. Babayigit, J. D'Haen, L. D'Olieslaeger, A. Ethirajan, J. Verbeeck, J. Manca, E. Mosconi, F. D. Angelis and H.-G. Boyen, *Adv. Energy Mater.*, 2015, **5**, 1500477.
- 39 S. Jaffar, K. T. Nam, A. Khademhosseini, J. Xing, R. S. Langer and A. M. Belcher, *Nano Lett.*, 2004, **4**, 1421–1425.
- 40 C. B. Murray, C. R. Kagan and M. G. Bawendi, *Annu. Rev. Mater. Sci.*, 2000, **30**, 545–610.
- 41 D. V. Talapin, J.-S. Lee, M. V. Kovalenko and E. V. Shevchenko, *Chem. Rev.*, 2010, **110**, 389–458.
- 42 A. R. Tao, J. Huang and P. Yang, *Acc. Chem. Res.*, 2008, **41**, 1662–1673.
- 43 H. M. Nguyen, O. Seitz, Y. N. Gartstein, Y. J. Chabal and A. V. Malko, *J. Opt. Soc. Am. B*, 2013, **30**, 2401–2408.
- 44 R. R. Chance, A. Prock and R. Silbey, in *Advances in Chemical Physics*, ed. S. A. Rice and I. Prigogine, Wiley, New York, 1978, vol. 37, pp. 1–65.
- 45 L. Novotny and B. Hecht, *Principles of Nano-Optics*, Cambridge University Press, Cambridge, 2006.
- 46 S. M. Rupich, Y. N. Gartstein, A. V. Malko and Y. J. Chabal, *Adv. Opt. Mater.*, 2016, **4**, 378–383.
- 47 W. J. I. De Benedetti, M. T. Nimmo, S. M. Rupich, L. M. Caillard, Y. N. Gartstein, Y. J. Chabal and A. V. Malko, *Adv. Funct. Mater.*, 2014, **24**, 5002–5010.
- 48 P. Löper, M. Stuckelberger, B. Niesen, J. Werner, M. Filipič, S.-J. Moon, J.-H. Yum, M. Topič, S. De Wolf and C. Ballif, *J. Phys. Chem. Lett.*, 2015, **6**, 66–71.
- 49 M. A. Green and M. J. Keevers, *Prog. Photovoltaics*, 1995, **3**, 189–192.
- 50 V. M. Agranovich, D. M. Basko, G. C. La Rocca and F. Bassani, *J. Phys.: Condens. Matter*, 1998, **10**, 9369–9400.